Comparative Study on the Localized Surface Plasmon Resonance of Boron- and Phosphorus-Doped Silicon Nanocrystals

Shu Zhou,[†,‡] Xiaodong Pi,[*,†] Zhenyi Ni,[†] Yi Ding,[‡] Yingying Jiang,[†] Chuanhong Jin,[†] Christophe Delerue,[§] Deren Yang,[*,†] and Tomohiro Nozaki[*,‡]

[†]State Key Laboratory of Silicon Materials and School of Materials Science and Engineering, Zhejiang University, Hangzhou, Zhejiang 310027, China, [‡]Department of Mechanical Science and Engineering, Tokyo Institute of Technology, Meguro, Tokyo 152-8550, Japan, and [§]IEMN-Département ISEN, UMR CNRS 8520, Lille 59046, France

ABSTRACT Localized surface plasmon resonance (LSPR) of doped Si nanocrystals (NCs) is critical to the development of Si-based plasmonics. We now experimentally show that LSPR can be obtained from both B- and P-doped Si NCs in the mid-infrared region. Both experiments and calculations demonstrate that the Drude model can be used to describe the LSPR of Si NCs if the dielectric screening and carrier effective mass of Si NCs are considered. When the doping levels of B and P are similar, the LSPR energy of B-doped Si NCs is higher than that of P-doped Si NCs because B is more efficiently activated to produce free carriers than P in Si NCs. We find that the plasmonic coupling between Si NCs is effectively blocked by oxide at the NC surface. The LSPR quality factors of B- and P-doped Si NCs approach those of traditional noble metal NCs. We demonstrate that LSPR is an effective means to gain physical insights on the electronic properties of doped Si NCs. The current work on the model semiconductor NCs, *i.e.*, Si NCs has important implication for the physical understanding and practical use of semiconductor NC plasmonics.

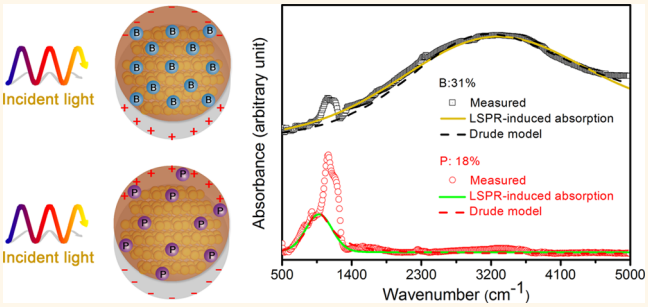

KEYWORDS: silicon · nanocrystals · localized surface plasmon resonance · boron · phosphorus

Impressive progress on the development of localized surface plasmon resonance (LSPR) has recently been made by using semiconductor nanocrystals (NCs).[1−7] In contrast to conventional noble metal NCs, semiconductor NCs greatly facilitate the integration of plasmonics with electronics.[8,9] Given the dominant role of silicon (Si) in electronics, the LSPR of Si NCs is highly desired for the plasmonics-electronics integration.[10,11] Rowe *et al.*[12] have recently demonstrated the LSPR of phosphorus (P)-doped Si NCs, leading to an intriguing question whether LSPR also occurs to boron (B)-doped Si NCs. It is well-known that B and P introduce free holes and electrons in Si materials, respectively. Since holes can behave differently from electrons, one may expect differences in the LSPR between B- and P-doped Si NCs if the LSPR of B-doped Si NCs also indeed exist. In addition, it has been shown that B prefers entering the core of a Si NC, while P prefers residing at the surface of a Si NC.[13−17] This leads to an important question whether the preferential doping impacts the LSPR of doped Si NCs. Therefore, a comparative study between B- and P-doped Si NCs in the context of LSPR is currently imperative.

In this work, we focus on Si NCs that are doped with B and P at high concentrations. LSPR in the energy regions of 0.26−0.40 eV and 0.09−0.13 eV has been found in B- and P-doped Si NCs, respectively. We clearly show that the LSPR energy increases with the increase of the dopant concentration, highlighting the remarkable doping-enabled tunability of LSPR for semiconductor NCs. The optical absorption of B- and P-doped Si NCs can be well simulated by using the Drude model.[18] We find that the

* Address correspondence to xdpi@zju.edu.cn, mseyang@zju.edu.cn, tnozaki@mech.titech.ac.jp.

Received for review September 24, 2014 and accepted December 31, 2014.

Published online December 31, 2014
10.1021/nn505416r

© 2014 American Chemical Society

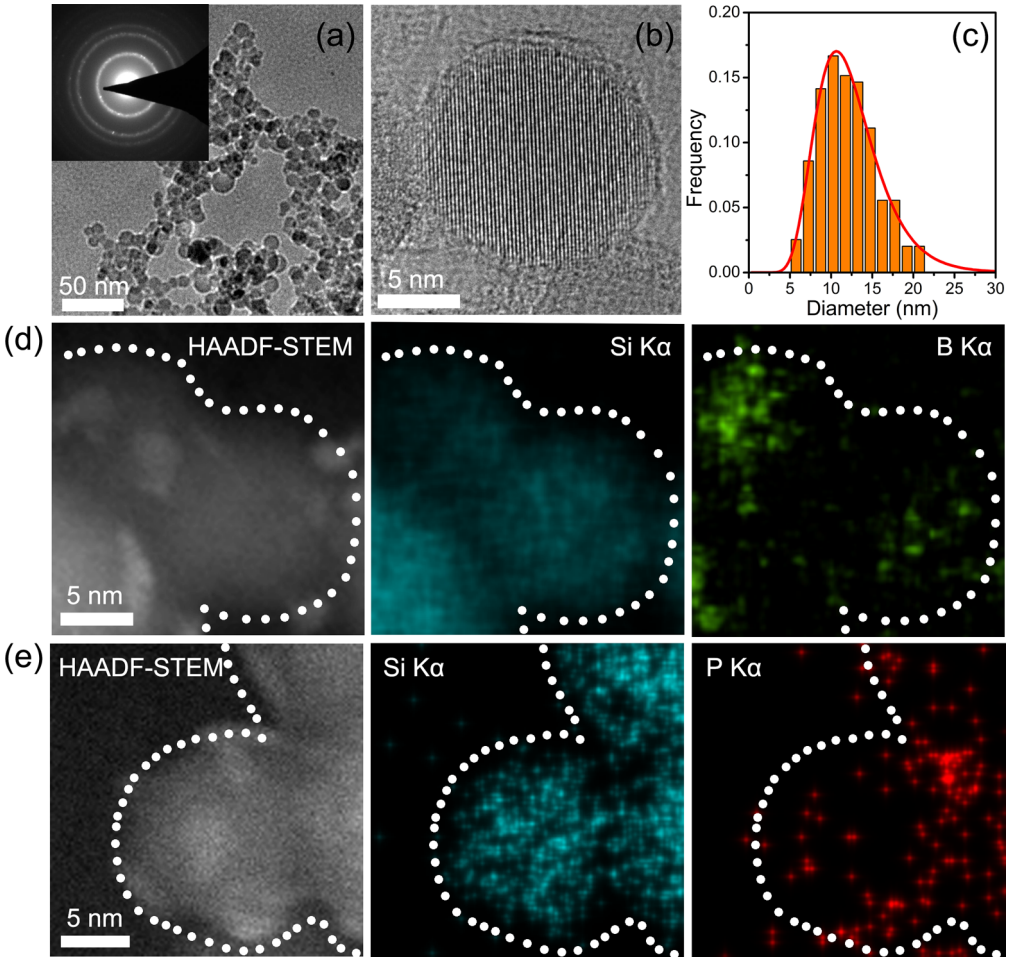

Figure 1. TEM images for undoped and doped Si NCs. (a) Low-resolution TEM image for undoped Si NCs. Inset of (a) shows the selected area electron diffraction (SAED) image. (b) Typical high-resolution TEM image for undoped Si NCs. (c) Size distribution for undoped Si NCs with a log-normal fit. The mean size is ~13 nm. (d) HAADF-STEM image and corresponding Si and B mapping images for Si NCs doped with 31% B. (e) HAADF-STEM image and corresponding Si and P mapping images for Si NCs doped with 18% P. Areas where Si NCs are located are approximately marked to guide the eye in (d) and (e).

plasmonic coupling between Si NCs is negligible because of oxide at the NC surface. We point out that the differences in LSPR between B- and P-doped Si NCs are basically related to the dopant distribution and free carrier behavior.

RESULTS AND DISCUSSION

Both undoped and doped Si NCs are synthesized by means of nonthermal plasma.[19,20] A series of measurements have been carried out to characterize all the Si NCs. Briefly, the structural properties of all the Si NCs are characterized by transmission electron microscopy (TEM) and X-ray diffraction (XRD). The concentration of B or P in an ensemble of Si NCs is obtained by using chemical titration. X-ray photoelectron spectroscopy (XPS) is employed to characterize the oxidation of Si NCs in air. Fourier transform infrared (FTIR) spectroscopy is used to study the absorption of all the Si NCs in the infrared region.

Structure Characterization. Figure 1a–c shows the TEM results for undoped Si NCs. Sphere-like undoped Si NCs are clearly seen in the low-resolution TEM image (Figure 1a). Selected-area electron diffraction (SAED) demonstrates the excellent crystallinity of undoped Si NCs (inset of Figure 1a). Figure 1b representatively shows the lattice fringes of an undoped Si NC. It is found that a log-normal curve may be used to fit the size distribution of undoped Si NCs, the mean size of which is ~13 nm (Figure 1c). This mean NC size is similar to that obtained by XRD analysis (Figure S1 in the Supporting Information). We do not see significant changes in the NC size when Si NCs are doped with B and P (Figures S1 and S2 in the Supporting Information). Doped Si NCs remain crystalline (Figures S1 and S2 in the Supporting Information). Chemical titration measurements show that in the current work Si NCs are doped with B and P in the concentration ranges of 7%–31% and 4%–18%, respectively. Such high concentrations of B/P may actually mean that Si–B/P alloys are produced. However, we just stick to the traditional term of doping for convenience. Figure 1d,e representatively shows the high-angle annular dark field (HAADF) scanning TEM images of Si NCs doped with B at the concentration of 31% and those doped with P at the concentration of 18%,

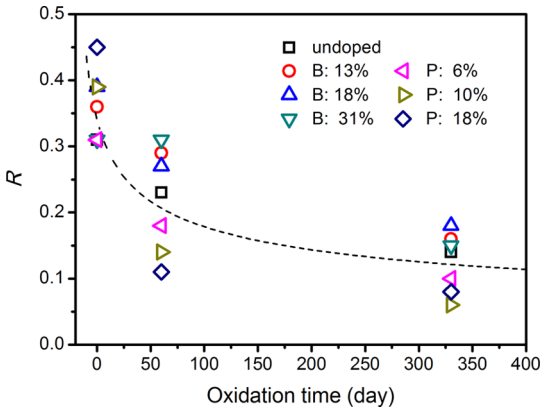

Figure 2. Ratio (*R*) of the number of Si atoms in intermediated oxidation states (Si^{1+}, Si^{2+} and Si^{3+}) to that of Si atoms in the neutral state and all oxidation states (Si^{1+}, Si^{2+}, Si^{3+} and Si^{4+}) obtained from XPS spectra of undoped and doped Si NCs. All the Si NCs are first measured shortly after exposure to air. They are then measured after ~60 and 330 days storage in air. The concentrations of P are 6%, 10%, and 18%, while those of B are 13%, 18%, and 31%. The dashed line is drawn to guide the eye.

respectively. Both of them indicate that the elements of B and P are associated with the element of Si. Si NCs are indeed doped with B and P. The successful doping for Si NCs has also been recently imaged by means of laser-assisted atom probe tomography.[21]

Localized Surface Plasmon Resonance. For all the as-synthesized Si NCs, we do not observe clear absorption peaks related to LSPR. This may be due to the fact that all the as-synthesized Si NCs are shortly exposed to air when FTIR spectroscopy measurements are carried out. The initial oxidation of Si NCs in air introduces a high density defects such as dangling bonds at the Si/oxide interface.[22,23] These interface defects may trap dopant-induced free carriers,[16,24,25] and hence void the LSPR. Figure 2 shows the ratio (*R*) of the number of Si atoms in intermediate oxidation states to that of Si atoms in the neutral state and all oxidation states. It is seen *R* decreases with the increase of oxidation time in air. It is known that a smaller value of R means a less defective Si/oxide interface.[26] Therefore, we believe that the density of defects at the Si/oxide interface is significantly reduced after Si NCs are oxidized in air for a long time. We would like to point out that the current improvement of the Si/oxide interface by means of long-time oxidation in air may be not efficient enough for practical use. More efficient oxidation methods such as ozone-enabled chemical oxidation need to be investigated in the future.[27]

FTIR spectroscopy measurements are carried out again for both undoped and doped Si NCs when they are oxidized in air for a long time (~330 days). Figure 3 shows the obtained FTIR spectra (assignments of the vibration modes in FTIR spectroscopy are shown in Table S1 in the Supporting Information). The oxidation of all the Si NCs is evidenced by the absorption peaks at ~1100 and 1200 cm^{-1}, which are associated with the vibration of Si−O−Si bonds.[28] It is clear that a broad

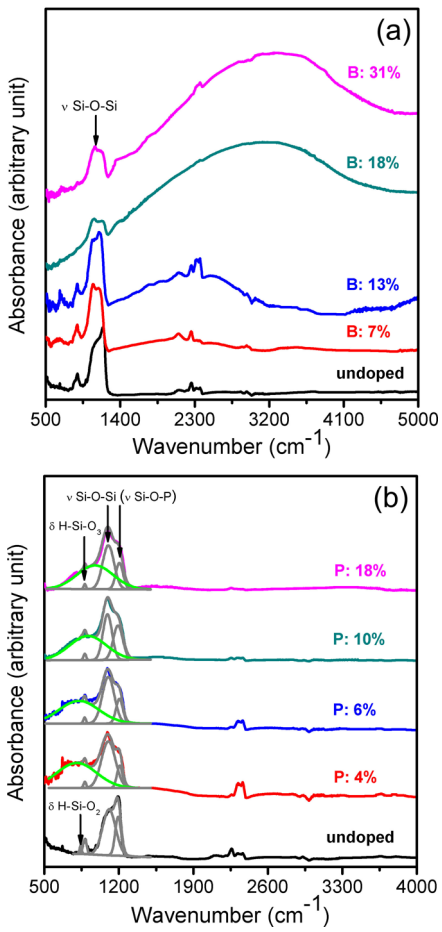

Figure 3. (a) FTIR spectra for undoped and B-doped Si NCs. (b) FTIR spectra for undoped and P-doped Si NCs. The FTIR spectrum for undoped Si NCs is fitted by four peaks located at ~850, 880, 1100, and 1200 cm^{-1}, while the FTIR spectrum of each P-doped Si-NC sample is fitted by three peaks at ~880, 1100, and 1200 cm^{-1} together with a fourth peak (green line). All the spectra are obtained after Si NCs are stored in air for ~330 days.

absorption peak emerges as Si NCs are doped with B (Figure 3a). The broad absorption peak moves from ~2090 to 3244 cm^{-1} when the B concentration increases from 7% to 31%. The dependence of the absorption energy on the doping level of B and the absence of the absorption for undoped Si NCs strongly suggest that B-doping-induced free holes lead to LSPR in Si NCs.

For P-doped Si NCs, the absorption related to Si−O−Si bonds and Si−O−P bonds (these two types of bonds are similar because of the similarity of P atoms to Si atoms) dominates all the FTIR spectra. However, we do observe a broad shoulder at the low-wavenumber side of the Si−O−Si/Si−O−P related absorption in the FTIR spectrum of each P-doped Si-NC sample. It is found that the FTIR spectrum of undoped Si NCs in the range below 1500 cm^{-1} can be fitted with four peaks, which are located at ~850, 880, 1100, and 1200 cm^{-1}. Among these four peaks, the peaks at ~850 and 880 cm^{-1} are associated with the

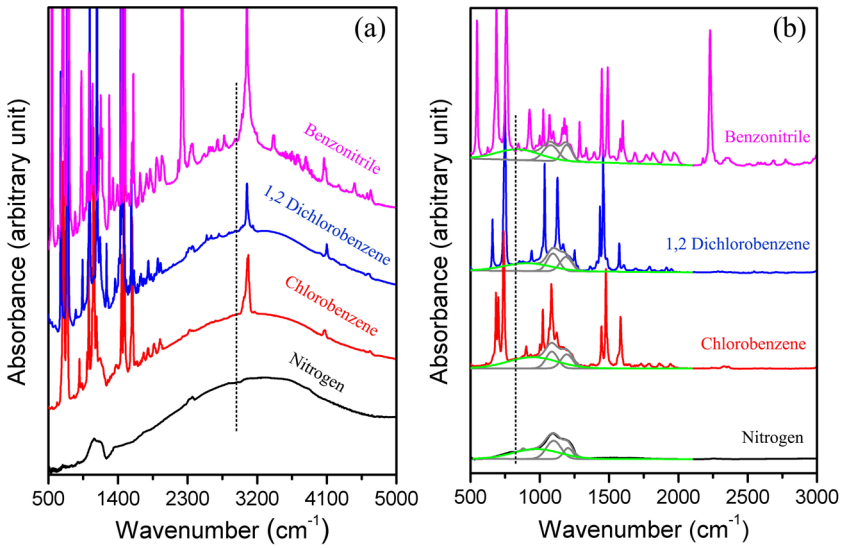

Figure 4. FTIR spectra for (a) B- and (b) P-doped Si NCs in different surrounding media, which are benzonitrile, 1,2 dichlorobenzene, chlorobenzene, and nitrogen with the dielectric constants of 25, 9.9, 5.6, and 1, respectively. The dopant concentrations of B and P are 31% and 18%, respectively. Each spectrum for P-doped Si NCs is fitted by two peaks located at ~1100 and 1200 cm^{-1} together with a third peak (green line), which corresponds to the LSPR-induced absorption. The dashed lines are used to facilitate the observation on the shifts of the LSPR-induced absorption.

vibration of H−Si−O_2 and H−Si−O_3 bonds,[29] respectively. Since the oxidation of Si NCs is enhanced by P doping,[13,14] H−Si−O_2 bonds hardly exist in oxidized P-doped Si NCs. But H−Si−O_3 bonds remain in oxidized P-doped Si NCs. Therefore, three peaks located at 880, 1100, and 1200 cm^{-1} are employed to fit the FTIR spectrum of each P-doped Si-NC sample in the range below 1500 cm^{-1} together with a fourth peak, which corresponds to the above-mentioned broad shoulder. It is interesting that the position of the fourth peak (broad shoulder) changes from ~804 to 977 cm^{-1} as the concentration of P increases from 4% to 18%. This indicates that P-doping-induced free electrons also give rise to LSPR in Si NCs. Please note that we have also obtained the FTIR spectra of P-doped Si NCs in the atmosphere of nitrogen after oxide at the NC surface is removed by HF vapor etching. The LSPR absorption has been clearly seen in these FTIR spectra without the interference of absorption induced by the vibration of O-related bonds (Figure S3 in the Supporting Information).

To further prove that LSPR occurs to both B- and P-doped Si NCs, we have examined the dependence of the LSPR energy on the surrounding medium. Si NCs doped with B at the concentration of 31% and those doped with P at the concentration of 18% are initially dispersed in benzonitrile, 1,2 dichlorobenzen and chlorobenzen with the same concentration. Each of these dispersions is then drop-cast onto a thallium bromoiodide (KRS-5) substrate for a FTIR measurement, which is carried out immediately after the drop casting. This means that the surrounding media of Si NCs are the solvents during the FTIR measurements. The dielectric constants of benzonitrile, 1,2 dichlorobenzene and chlorobenzene are 25, 9.9 and 5.6, respectively.[30] When the solvents totally evaporate, the surrounding media of Si NCs are changed to be nitrogen, which has a dielectric constant of 1. Hence, we should expect changes in LSPR energy according to the relationship between the LSPR energy ($\hbar\omega_{sp}$) and dielectric constant (ε_m) of the surrounding medium of Si NCs:[31]

$$\hbar\omega_{sp} \approx \hbar\sqrt{\frac{ne^2}{\varepsilon_0 m^*(\varepsilon_\infty + 2\varepsilon_m)}} \quad (1)$$

where n is the free carrier concentration, e is the electronic charge, ε_0 is the free space permittivity, m^* is the effective mass of a free carrier (0.3 m_0 for an electron and 0.4 m_0 for a hole), ε_∞ is the high frequency dielectric constant of a Si NC. Please note that the carrier damping constant (Γ) is not incorporated in the Drude theory based eq 1 because it is usually small enough not to seriously affect ω_{sp}. eq 1 was theoretically validated for P-doped Si NCs in our previous work.[31] In the current work we have further found that eq 1 is also applicable to B-doped Si NCs by means of tight-binding calculations (Figures S4 and S5 in the Supporting Information).

Figure 4 shows the FTIR spectra for (a) B- and (b) P-doped Si NCs with the varying surrounding medium. The solvents around Si NCs are manifested by the intense sharp absorption peaks in the FTIR spectra. As the dielectric constant of the surrounding medium decreases from 25 to 1, we see that the LSPR-induced absorption of B- and P-doped Si NCs blueshifts from ~2940 to 3145, 3200. and 3244 cm^{-1} and from ~830 to 910, 949, and 977 cm^{-1}, respectively. These changes in the LSPR energy are consistent with those predicted by using eq 1, in which an effective dielectric constant (ε_{eff}) is adopted to substitute ε_∞ for the sake of taking into account the screening effect of oxide at the NC

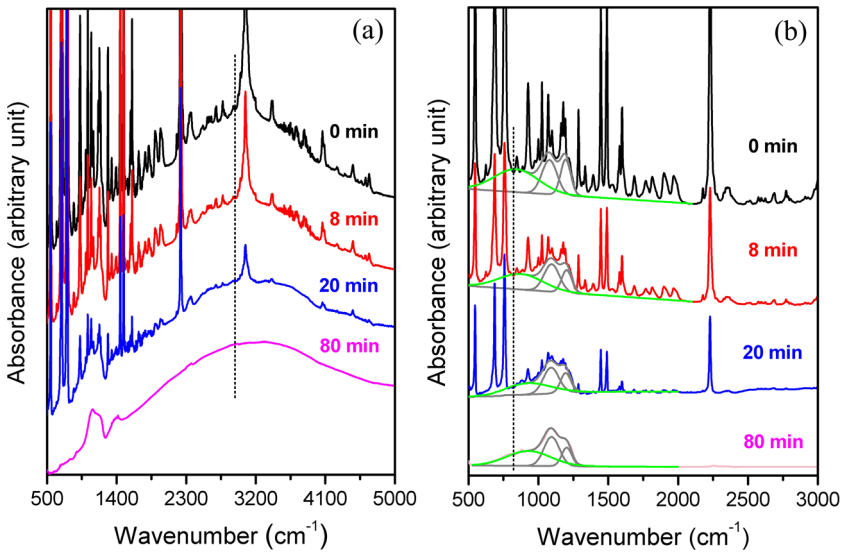

Figure 5. FTIR spectra for (a) B- and (b) P-doped Si NCs exhibiting shifts upon the solvent (benzonitrile) evaporation with different time. The dopant concentration is 31% for B and 18% for P. The absorption arising from P-doped Si NCs in (b) is fitted by two peaks located at ~1100 and 1200 cm^{-1} together with a third peak (green line) corresponding to the LSPR-induced absorption. The dashed lines are used to facilitate the observation on the shifts of the LSPR-induced absorption.

surface (Figure S7 in the Supporting Information).[32] We would like to point out that the ignorance of the oxide at the NC surface causes the values of the LSPR energy predicted by eq 1 to be smaller than those measured. This indicates that the dielectric screening of the oxide at the NC surface does exist. But it is clear that the oxide at the NC surface does not render complete dielectric screening. The LSPR of our doped Si NCs with oxide at the NC surface is reasonably sensitive to their environments.

Plasmonic Coupling. All the samples for FTIR measurements are prepared by drop casting in the current work. After solvent evaporation Si NCs aggregate. According to previous work on noble metal NCs,[5,33] we may expect that the aggregation of Si NCs likely leads to plasmonic coupling between Si NCs. Figure 5 shows the FTIR spectra for Si NCs doped with 31% B and 18% P collected during the course of the evaporation of benzonitrile. When benzonitrile nearly completely evaporates after 80 min, the LSPR-induced absorption blueshifts from ~2940 cm^{-1} to 3240 cm^{-1} and from ~830 cm^{-1} to 940 cm^{-1} for B- and P-doped Si NCs, respectively. This means that plasmonic coupling between Si NCs is negligible despite the solvent-evaporation-induced aggregation of Si NCs, since plasmonic coupling usually gives rise to the redshift of LSPR-induced absorption.[34−36] Clearly, the observed blueshift of the LSPR-induced absorption is largely due to the change of the surrounding medium from benzonitrile to nitrogen.

We have previously shown that after long-time room-temperature oxidation the thicknesses of surface oxide are ~1.4 and 2.7 nm for Si NCs doped with 31% B and 18% P, respectively.[14] Hence, we can work out that the shortest distances between Si NCs are ~2.8 and 5.4 nm for Si NCs doped with 31% B and 18% P, respectively. These shortest NC−NC distances are larger than 20% of the diameter of Si NCs (~2.6 nm). Because near-field plasmonic coupling significantly decays as the NC−NC distance is larger than 20% of the NC size,[34−36] we can readily understand the negligible plasmonic coupling indicated by Figure 5. We would like to mention that we have also collected FTIR spectra for HF-vapor-etched Si NCs that are doped with 31% B and 18% P during the course of the evaporation of benzonitrile (Figure S6 in the Supporting Information). When benzonitrile totally evaporates, the LSPR-induced absorption does redshift for both B- and P-doped Si NCs. It is apparent that the lack of oxide at the NC surface causes the distances between Si NCs to be small enough to enable strong plasmonic coupling when Si NCs aggregate.

Carrier Mobility. We find that all the LSPR-induced absorption peaks can be well fitted by assuming that the Mie absorption of Si NCs includes the Drude contribution, which is expressed by

$$\sigma_A(\omega) = \frac{8\pi^2\sqrt{\varepsilon_m}r^3\omega}{c}\mathrm{Im}\left\{\frac{\varepsilon(\omega) - \varepsilon_m}{\varepsilon(\omega) + 2\varepsilon_m}\right\} \quad (2)$$

where $\sigma_A(\omega)$ is the absorption cross section of a Si NC at the frequency of ω, c is the speed of light, r is the NC radius and $\varepsilon(\omega)$ is the frequency-dependent dielectric constant of the NC. $\varepsilon(\omega)$ is given by the well-known Drude equation:

$$\varepsilon(\omega) = \varepsilon_\infty - \frac{\omega_{p^2}}{\omega^2 + i\omega\Gamma} \quad (3)$$

where ω_p is the bulk plasma frequency. Please note that the validity of eq 2 is justified by the surface-oxide-induced negligible plasmonic coupling between Si NCs. Figure 6a representatively shows the good fitting for Si NCs doped with 31% B and 18% P. Please note that Γ and ω_p are readily obtained from the fitting

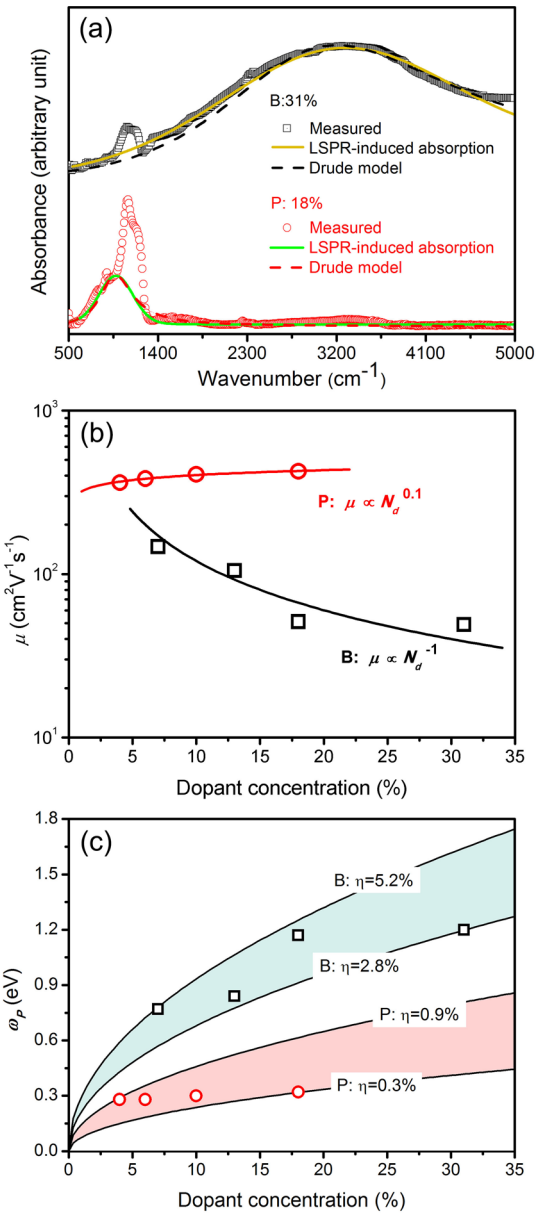

Figure 6. (a) Fitting of the LSPR-induced absorption for Si NCs doped with 31% B and that for Si NCs doped with 18% P by using the Drude model. (b) Carrier mobility (μ) of each doped Si-NC sample obtained by fitting the LSPR-induced absorption peak. The black line gives $\mu \propto N_d^{-1}$, while the red line gives $\mu \propto N_d^{0.1}$, where N_d is the dopant concentration. (c) Bulk plasma frequency (ω_p) *versus* dopant concentration (N_d). The solid lines represent the fitting by using $\omega_p = [N_d\eta e^2/(m^*\varepsilon_0)]^{1/2}$. The values of dopant activation efficiency (η) obtained from the fitting are indicated.

(Table S2 in the Supporting Information). We find that Γ increases from ~1000 to 3000 cm^{-1} as the concentration of B increases from 7% to 31%. But Γ slightly decreases from ~540 to 460 cm^{-1} when the concentration of P increases from 4% to 18%. It is known that $\mu = he/(m^*\Gamma)$, where μ and h are the carrier mobility and Planck constant (Γ is deemed as energy), respectively.[37] Therefore, we can then work out the carrier mobility of each doped Si-NC sample. Figure 6b shows the carrier mobility of each doped Si-NC sample obtained by fitting the LSPR-induced absorption peak. We see that the hole mobility decreases from ~150 to 50 $cm^2V^{-1}s^{-1}$ as the concentration of B increases from 7% to 31%. Such an inversely proportional dependence of the hole mobility on the concentration of B indicates that holes are predominantly scattered by ionized B atoms in Si NCs, similar to what occurs in bulk Si.[38] In contrast, the electron mobility for P-doped Si NCs increases from ~360 to 425 $cm^2\ V^{-1}\ s^{-1}$ with the increase of the concentration of P from 4% to 18%. By using

$$L = h\sqrt{3KT/m^*}/\Gamma \tag{4}$$

where L, K and T are the mean free path of carriers, Boltzmann constant and temperature (300 K), respectively, we estimate that the mean free paths of holes in B-doped Si NCs and electrons in P-doped Si NCs are 2−7 and 12−15 nm, respectively. Since the mean free paths of electrons basically approximate to the NC size, the surface scattering of electrons in P-doped Si NCs should be more significant than that of holes in B-doped Si NCs. When P atoms are at the NC surface, they may be not ionized. In addition, P atoms are more electronegative than Si atoms. Hence, un-ionized P atoms at the NC surface can retard the movement of electrons toward the NC surface, reducing the surface scattering of electrons. The increase of the concentration of P may mainly lead to more P atoms at the NC surface, making the surface scattering of electrons less effective. Therefore, it turns out that the mobility of electrons in P-doped Si NCs can increase when the concentration of P increases.

We would like to point out that the values of the carrier mobility derived from the current optical measurements are comparable with those of doped bulk Si obtained by Hall measurements,[39] but several orders of magnitude higher than those of B- and P-doped Si-NC films in field-effect transistors.[40] This implies that carrier transport in a Si-NC film is mainly limited by the tunneling between neighboring Si NCs.

Dopant Activation Efficiency. The bulk plasma frequency (ω_p) derived from the fitting of LSPR-induced absorption is related to the free carrier concentration (n) *via* $\omega_p^2 = ne^2/(m^*\varepsilon_0)$. The free carrier concentration obtained with this expression is quite comparable with that obtained by using eq 1 (Table S3 in the Supporting Information). This further experimentally validates eq 1 for Si NCs. Since n depends on the activation efficiency (η) of B or P in Si NCs with a concentration of N_d ($n = N_d\eta$), we can obtain the value of η by fitting the ω_p−N_d data according to

$$\omega_p = \sqrt{\frac{N_d\eta e^2}{m^*\varepsilon_0}} \tag{5}$$

The results are shown in Figure 6c. It is seen that the values of the activation efficiency of B and P are 2.8% −5.2% and 0.3%−0.9%, respectively. Clearly, B much

more efficiently produces free carriers than P in Si NCs. We should mention that in the current study Si NCs are heavily doped in terms of free carrier concentrations (up to 4×10^{20} cm^{-3} and 3×10^{19} cm^{-3} for B- and P-doped Si NCs, respectively), although B and P have been hyperdoped to concentrations exceeding their solubility in Si.[41] It looks that the distribution of dopants in Si NCs is not the only factor that determines the activation of dopants. Although B prefers residing in the NC core, significant portion of B atoms remain electrically inactive. The trend of the decrease of the activation efficiency with the increase of the dopant concentration for both B and P indicates that the clustering of B and P may become serious as their concentrations increase.[42−44] Future work is needed to minimize the deactivation of B and P in Si NCs, moving the LSPR of Si NCs toward the visible region.

Quality Factor of LSPR. Finally, we calculate the quality factor (Q) of the LSPR of doped Si NCs by using

$$Q = \omega_{sp}/\gamma \tag{6}$$

where γ is the line width (half width at the half-maximum) of a LSPR-induced absorption peak. We notice that the values of γ for B-doped Si NCs are larger than those for P-doped Si NCs in the current work. The value of γ usually increases with the increase of the scattering of carriers.[2,45] As mentioned before, B atoms are more efficiently activated (ionized) to produce free carriers than P atoms. This means that the scattering of carriers by ionized impurities may be more significant in B-doped Si NCs than that in P-doped Si NCs. Therefore, it is reasonable that the values of γ for B-doped Si NCs are larger than those for P-doped Si NCs. Moreover, it is known that the scattering of carriers by twin boundaries may also contribute to the broadening of a LSPR-induced absorption peak.[12] We have previously demonstrated that twin defects may occur to both B- and P-doped Si NCs with high doping levels.[14] The number of twin boundaries in a B-doped Si NC is often larger than that in a P-doped Si NC, probably due to the larger difference in the atom size between a B atom and a Si atom. The larger numbers of twin boundaries should also contribute to the broader LSPR-induced absorption peaks for B-doped Si NCs.

Despite the larger values of γ for B-doped Si NCs the values of Q for B-doped Si NCs is actually not significantly smaller than those for P-doped Si NCs because the values of ω_{sp} for B-doped Si NCs are also larger. The values of Q for B-doped Si NCs are about 3−4, while those for P-doped Si NCs are about 4−5. Therefore, we may state that the values of Q for our doped Si NCs may be higher than those for other semiconductor NCs such as copper chalcogenide NCs,[46] tungsten oxide NCs[6] and indium tin oxide NCs,[47] approaching those for traditional noble metal NCs.[48] This brings great promise for the use of doped Si NCs in a variety of demanding plasmonic applications such as highly sensitive chemical sensing.[49] We have complied the values of γ for current B- and P-doped Si NCs and those reported by Rowe *et al.* for P-doped Si NCs (Figure S8 in the Supporting Information). It is found that the value of γ for B-doped Si NCs is smaller than that for P-doped Si NCs when their LSPR energies are similar. This implies that the value of Q for B-doped Si may be larger than that for P-doped Si NCs in the same LSPR energy region.

CONCLUSIONS

In summary, we have demonstrated the LSPR of B-doped Si NCs for the first time. The LSPR of B-doped Si NCs has been systematically compared with that of P-doped Si NCs. It is found that the LSPR energies for B- and P-doped Si NCs are now all located at mid-infrared region. But the LSPR energy of B-doped Si NCs is larger than that of P doped Si NCs when the doping levels of B and P are similar. This is because B is much more efficiently activated than P in Si NCs. By fitting the LSPR-induced absorption of both B- and P-doped Si NCs with the Drude model, the values of the hole/electron mobility for Si NCs have been obtained. It is seen that the hole mobility decreases with the increase of the B concentration of Si NCs. However, the electron mobility slightly increases with the increase of the P concentration of Si NCs. All the differences between B- and P-doped Si NCs may be related to dopant distribution, which impacts the dopant activation and carrier scattering. The LSPR quality factors of B and P doped Si NCs are approaching those of traditional noble metal NCs, signifying the great potential of doped Si NCs in plasmonic applications. Oxide at the NC surface is found to effectively block the plasmonic coupling between Si NCs. It looks that B-doped Si NCs are better positioned for practical use than P-doped Si NCs. On one hand, B atoms can be more efficiently activated than P atoms, enabling greater tunability of LSPR for B-doped Si NCs than P-doped Si NCs. On the other hand, the LSPR of B-doped Si NCs may be not as seriously screened by the vibration of O-related bonds as that of P-doped Si NCs. We hope that the current experimental progress on the LSPR of doped Si NCs should encourage the development of novel Si-based plasmonic devices.[11,49]

METHODS

B and P-doped Si NCs were synthesized by introducing B_2H_6 (0.5% in Ar) and PH_3 (0.5% in Ar) into a SiH_4/Ar nonthermal plasma chamber, respectively. The flow rate of B_2H_6 (PH_3) was changed from 0.88 (1.77) standard cubic centimeters per minute (sccm) to 15.2 (30.3) sccm, while the flow rate of SiH_4 was kept at 31.5 sccm. The total gas flow rate was fixed at ∼3820 sccm and the pressure was maintained at ∼360 Pa

for synthesizing all the Si NCs. A 13.56 MHz power source and a matching network were used to generate the plasma. The power for synthesizing all the Si NCs was ~200 W.

For measuring the B (P) concentration of Si NCs, Si NCs doped with B (P) were initially reacted with KOH in a nickel crucible. The product was then transferred to a plastic cup. HNO_3 was added into the plastic cup to form silicic and boracic (phosphoric) acids. Excessive potassium chloride and potassium fluoride were added to precipitate potassium fluorosilicate and potassium fluoroborate (fluorophosphate). These precipitates were then hydrolyzed in water, leading to the formation of HF. The resulting solution was treated by a standard NaOH titration method. Phenolphthalein was used to indicate the end of titration.

TEM measurements were performed by FEI Tecnai G2 F20 S-TWIN with an acceleration voltage of 200 kV. HAADF-STEM and element mapping measurements were performed by FEI Titan G2 80−200 w/Chemi STEM with an acceleration voltage of 200 kV. Si NCs were dispersed in ethanol by ultrasonication after they were synthesized. Samples for both TEM and HAADF-STEM measurements were prepared by drop-casting the Si-NC-containing dispersion onto a carbon-coated copper grid. The copper grids were inserted to the microscope after ethanol totally evaporated.

XRD measurements were performed by X'Pert PRO. Si-NC powders were collected on a glass substrate inside the plasma synthesis system. X-rays generated by a Cu Kα source at the voltage of 40 V were employed. A scanning step of 0.016° was used for measuring all the Si-NC powder samples.

XPS measurements were performed by Kratos AXIS Ultra DLD. The samples for XPS were prepared by placing as-synthesized Si NCs on a 5 mm × 5 mm carbon-tape-covered aluminum substrate. They were measured within ~1 h exposure to air. The measurements were carried out again after Si NCs were exposed to air at room temperature for 2 and 11 months.

For a FTIR measurement, a Si-NC dispersion was prepared by the addition of ~10 mg of Si NCs into a 2 mL solvent (benzonitrile, 1,2 dichlorobenzene or chlorobenzene) and subsequent ultrasonication for 3 min with a tip-ultrasonicator (Sonic & Materials, Inc.-VCX130PB) at ~2 W. The Si-NC dispersion was then drop-casted onto a thallium bromoiodide substrate for the FTIR measurement in the transmission mode. A FTIR spectrum was collected either after the solvent totally evaporated or during the course of the evaporation of the solvent. Nitrogen might be used to enable an inert atmosphere for a sample during the FTIR measurement. All the FTIR measurements were performed by using JASCO FT/IR-6100 with a resolution of 4 cm^{-1}.

Conflict of Interest: The authors declare no competing financial interest.

Supporting Information Available: XRD results for both undoped and doped Si NCs, TEM results for doped Si NCs, assignments of vibration modes, optical absorption of P-doped Si NCs after HF vapor etching, tight-binding calculation of the optical absorption of B-doped Si NCs, plasmonic coupling of B- and P-doped Si NCs that are etched by HF vapor, parameters obtained by fitting the LSPR-induced absorption of B- and P-doped Si NCs, free carrier concentrations calculated by using eq 1 or fitting the LSPR-induced absorption and quality of LSPR in B- and P-doped Si NCs. This material is available free of charge *via* the Internet at http://pubs.acs.org.

Acknowledgment. This work is mainly supported by the National Basic Research Program of China (Grant Nos. 2013CB632101, 2014CB932500 & 2015CB921000) and the NSFC for excellent young researchers (Grant Nos. 61222404 & 51222202). Partial support from the R&D Program of Ministry of Education of China (Grant No. 62501040202) and the Fundamental Research Funds for the Central Universities (2014XZZX003-09) is acknowledged. The Center for Electron Microscopy of Zhejiang University is acknowledged for providing TEM characterization.

REFERENCES AND NOTES

1. Liu, X.; Swihart, M. T. Heavily-Doped Colloidal Semiconductor and Metal Oxide Nanocrystals: An Emerging New Class of Plasmonic Nanomaterials. *Chem. Soc. Rev.* **2014**, *43*, 3908–3920.
2. Luther, J. M.; Jain, P. K.; Ewers, T.; Alivisatos, A. P. Localized Surface Plasmon Resonances Arising from Free Carriers in Doped Quantum Dots. *Nat. Mater.* **2011**, *10*, 361–366.
3. Polking, M. J.; Jain, P. K.; Bekenstein, Y.; Banin, U.; Millo, O.; Ramesh, R.; Alivisatos, A. P. Controlling Localized Surface Plasmon Resonances in GeTe Nanoparticles Using an Amorphous-to-Crystalline Phase Transition. *Phys. Rev. Lett.* **2013**, *111*, 037401.
4. Garcia, G.; Buonsanti, R.; Runnerstrom, E. L.; Mendelsberg, R. J.; Llordes, A.; Anders, A.; Richardson, T. J.; Milliron, D. J. Dynamically Modulating the Surface Plasmon Resonance of Doped Semiconductor Nanocrystals. *Nano Lett.* **2011**, *11*, 4415–4420.
5. Naik, G. V.; Shalaev, V. M.; Boltasseva, A. Alternative Plasmonic Materials: Beyond Gold and Silver. *Adv. Mater.* **2013**, *25*, 3264–3294.
6. Manthiram, K.; Alivisatos, A. P. Tunable Localized Surface Plasmon Resonances in Tungsten Oxide Nanocrystals. *J. Am. Chem. Soc.* **2012**, *134*, 3995–3998.
7. Buonsanti, R.; Llordes, A.; Aloni, S.; Helms, B. A.; Milliron, D. J. Tunable Infrared Absorption and Visible Transparency of Colloidal Aluminum-Doped Zinc Oxide Nanocrystals. *Nano Lett.* **2011**, *11*, 4706–4710.
8. Ozbay, E. Plasmonics: Merging Photonics and Electronics at Nanoscale Dimensions. *Science* **2006**, *311*, 189–193.
9. Faucheaux, J. A.; Stanton, A. L. D.; Jain, P. K. Plasmon Resonances of Semiconductor Nanocrystals: Physical Principles and New Opportunities. *J. Phys. Chem. Lett.* **2014**, *5*, 976–985.
10. Soref, R. Mid-Infrared Photonics in Silicon and Germanium. *Nat. Photonics* **2010**, *4*, 495–497.
11. Walters, R. J.; Loon, R. V. A. van; Brunets, I.; Schmitz, J.; Polman, A. A Silicon-Based Electrical Source of Surface Plasmon Polaritons. *Nat. Mater.* **2010**, *9*, 21–25.
12. Rowe, D. J.; Jeong, J. S.; Mkhoyan, K. A.; Kortshagen, U. R. Phosphorus-Doped Silicon Nanocrystals Exhibiting Mid-Infrared Localized Surface Plasmon Resonance. *Nano Lett.* **2013**, *13*, 1317–1322.
13. Pi, X. D.; Gresback, R.; Liptak, R. W.; Campbell, S. A.; Kortshagen, U. Doping Efficiency, Dopant Location, and Oxidation of Si Nanocrystals. *Appl. Phys. Lett.* **2008**, *92*, 123102.
14. Zhou, S.; Pi, X. D.; Ni, Z. Y.; Luan, Q. B.; Jiang, Y. Y.; Jin, C. H.; Nozaki, T.; Yang, D. Boron- and Phosphorus-Hyperdoped Silicon Nanocrystals. *Part. Part. Syst. Charact.* **2014**, 10.1002/ppsc.201400103.
15. Chan, T. L.; Tiago, M. L.; Kaxiras, E.; Chelikowsky, J. R. Size Limits on Doping Phosphorus into Silicon Nanocrystals. *Nano Lett.* **2008**, *8*, 596–600.
16. Stegner, A. R.; Pereira, R. N.; Lechner, R.; Klein, K.; Wiggers, H.; Stutzmann, M.; Brandt, M. S. Doping Efficiency in Free-standing Silicon Nanocrystals from the Gas Phase: Phosphorus Incorporation and Defect-Induced Compensation. *Phys. Rev. B* **2009**, *80*, 165326.
17. Chen, X. B.; Pi, X. D.; Yang, D. R. Critical Role of Dopant Location for P-Doped Si Nanocrystals. *J. Phys. Chem. C* **2011**, *115*, 661–666.
18. Mendelsberg, R. J.; Garcia, G.; Li, H. B.; Manna, L.; Milliron, D. J. Understanding the Plasmon Resonance in Ensembles of Degenerately Doped Semiconductor Nanocrystals. *J. Phys. Chem. C* **2012**, *116*, 12226–12231.
19. Mangolini, L.; Thimsen, E.; Kortshagen, U. High-Yield Plasma Synthesis of Luminescent Silicon Nanocrystals. *Nano Lett.* **2005**, *5*, 655–659.
20. Pi, X. D.; Yu, T.; Yang, D. Water-Dispersible Silicon-Quantum-Dot-Containing Micelles Self-Assembled from an Amphiphilic Polymer. *Part. Part. Syst. Charact.* **2014**, *32*, 751–756.
21. Khelifi, R.; Mathiot, D.; Gupta, R.; Muller, D.; Roussel, M.; Duguay, S. Efficient N-Type Doping of Si Nanocrystals Embedded in SiO_2 by Ion Beam Synthesis. *Appl. Phys. Lett.* **2013**, *102*, 013116.
22. Gupta, A.; Schulz, C.; Wiggers, H. Influence of Etching and Surface Functionalization on the Optical Property of

Luminescing Phosphorus Doped Silicon Nanoparticles. *J. Optoelectron. Adv. Mater.* **2010**, *12*, 518–522.
23. Pi, X. D.; Liptak, R. W.; Campbell, S. A.; Kortshagen, U. In-Flight Dry Etching of Plasma-Synthesized Silicon Nanocrystals. *Appl. Phys. Lett.* **2007**, *91*, 083112.
24. Stirling, A.; Pasquarello, A.; Charlier, J. C.; Car, R. Dangling Bond Defects at Si-SiO_2 Interfaces: Atomic Structure of the P(b1) Center. *Phys. Rev. Lett.* **2000**, *85*, 2773–2776.
25. Delerue, C.; Allan, G.; Lannoo, M. Theoretical Aspects of the Luminescence of Porous Silicon. *Phys. Rev. B* **1993**, *48*, 11024–11036.
26. Himpsel, F. J.; Mcfeely, F. R.; Talebibrahimi, A.; Yarmoff, J. A.; Hollinger, G. Microscopic Structure of the SiO_2/Si Interface. *Phys. Rev. B* **1988**, *38*, 6084–6096.
27. Zhang, J.; Zou, H. J.; Qing, Q.; Yang, Y. L.; Li, Q. W.; Liu, Z. F.; Guo, X. Y.; Du, Z. L. Effect of Chemical Oxidation on the Structure of Single-Walled Carbon Nanotubes. *J. Phys. Chem. B* **2003**, *107*, 3712–3718.
28. Pi, X. D.; Mangolini, L.; Campbell, S. A.; Kortshagen, U. Room-Temperature Atmospheric Oxidation of Si Nanocrystals after HF Etching. *Phys. Rev. B* **2007**, *75*, 085423.
29. Yeh, J. L.; Lee, S. C. Structural and Optical Properties of Amorphous Silicon Oxynitride. *J. Appl. Phys.* **1996**, *79*, 656–663.
30. Wheeler, L. M.; Neale, N. R.; Chen, T.; Kortshagen, U. R. Hypervalent Surface Interactions for Colloidal Stability and Doping of Silicon Nanocrystals. *Nat. Commun.* **2013**, *4*, 2197–2206.
31. Pi, X. D.; Delerue, C. Tight-Binding Calculations of the Optical Response of Optimally P Doped Si Nanocrystals: A Model for Localized Surface Plasmon Resonance. *Phys. Rev. Lett.* **2013**, *111*, 177402.
32. Neeves, A. E.; Birnboim, M. H. Composite Structures for the Enhancement of Nonlinear-Optical Susceptibility. *J. Opt. Soc. Am. B* **1989**, *6*, 787–796.
33. Prashant, K. J.; Mostafa, A. E. Plasmonic Coupling in Noble Metal Nanostructures. *Chem. Phys. Lett.* **2010**, *487*, 153–164.
34. Prashant, K. J.; Huang, W. Y.; Mostafa, A. E. On the Universal Scaling Behavior of the Distance Decay of Plasmon Coupling in Metal Nanoparticle Pairs: A Plasmon Ruler Equation. *Nano Lett.* **2007**, *7*, 2080–2088.
35. Su, K. H.; Wei, Q. H.; Zhang, X.; Mock, J. K.; Smith, D. R.; Schultz, S. Interparticle Coupling Effects on Plasmon Resonances of Nanogold Particles. *Nano Lett.* **2003**, *3*, 1087–1090.
36. Su, W. H.; Charles, N.; Andrea, R. T. Tunable and Directional Plasmonic Coupling within Semiconductor Nanodisk Assemblies. *Nano Lett.* **2014**, *14*, 2372–2380.
37. Grant, J.; Shi, X.; Alton, J.; Cumming, D. R. S. Terahertz Localized Surface Plasmon Resonance of Periodic Silicon Microring Arrays. *J. Appl. Phys.* **2011**, *109*, 054903.
38. Sze, S. M. *Physics of Semiconductor Devices*; John Wiley & Sons: New York, 1969; p 39.
39. Masetti, G.; Severi, M.; Solmi, S. Modeling of Carrier Mobility against Carrier Concentration in Arsenic-Doped, Phosphorus-Doped, and Boron-Doped Silicon. *IEEE Trans. Electron Devices* **1983**, *30*, 764–769.
40. Gresback, R.; Kramer, N. J.; Ding, Y.; Chen, T.; Kortshagen, U. R.; Nozaki, T. Controlled Doping of Silicon Nanocrystals Investigated by Solution-Processed Field Effect Transistors. *ACS Nano* **2014**, *8*, 5650–5656.
41. Kodera, H. Constitutional Supercooling during the Crystal Growth of Germanium and Silicon. *Jpn. J. Appl. Phys.* **1963**, *2*, 527–534.
42. Sugimoto, H.; Fujii, M.; Imakita, K.; Hayashi, S.; Akamatsu, K. Phosphorus and Boron Codoped Colloidal Silicon Nanocrystals with Inorganic Atomic Ligands. *J. Phys. Chem. C* **2013**, *117*, 6807–6813.
43. Zeng, Y. H.; Ma, X. Y.; Tian, D. X.; Wang, W. Y.; Gong, L. F.; Yang, D. R.; Que, D. L. Oxygen Precipitation Heterogeneously Nucleating on Silicon Phosphide Precipitates in Heavily Phosphorus-Doped Czochralski Silicon. *J. Appl. Phys.* **2009**, *105*, 093503.
44. Landi, E.; Guimaraes, S.; Solmi, S. Influence of Nucleation on the Kinetics of Boron Precipitation in Silicon. *Appl. Phys. A: Mater. Sci. Process.* **1987**, *44*, 135–141.
45. Alberto, C.; Liberato, M. New Materials for Tunable Plasmonic Colloidal Nanocrystals. *Chem. Soc. Rev.* **2014**, *43*, 3957–3975.
46. Kriegel, I.; Jiang, C. Y.; Fernandez, J. R.; Schaller, R. D.; Talapin, D. V.; Como, E. D.; Feldmann, J. Tuning the Excitonic and Plasmonic Properties of Copper Chalcogenide Nanocrystals. *J. Am. Chem. Soc.* **2012**, *134*, 1583–1590.
47. Kanehara, M.; Koike, H.; Yoshinaga, T.; Teranishi, T. Indium Tin Oxide Nanoparticles with Compositionally Tunable Surface Plasmon Resonance Frequencies in the Near-IR Region. *J. Am. Chem. Soc.* **2009**, *131*, 17736–17737.
48. Rycenga, M.; Cobley, C. M.; Zeng, J.; Li, W. Y.; Moran, C. H.; Zhang, Q.; Qin, D.; Xia, Y. N. Controlling the Synthesis and Assembly of Silver Nanostructures for Plasmonic Applications. *Chem. Rev.* **2011**, *111*, 3669–3712.
49. Law, S.; Podolskiy, V.; Wasserman, D. Towards Nano-Scale Photonics with Micro-Scale Photons: the Opportunities and Challenges of Mid-Infrared Plasmonics. *Nanophotonics* **2013**, *2*, 103–130.